Soft Matter

Control over emergence and alignment of transient blisters in thermo-responsive gels using hierarchically patterned substrates

Journal:	*Soft Matter*
Manuscript ID	SM-ART-05-2022-000579.R1
Article Type:	Paper
Date Submitted by the Author:	19-Jul-2022
Complete List of Authors:	Liu, Ya; University of Pittsburgh, ; Zhang, Cathy; Harvard University, Aizenberg, Joanna; Harvard University, Balazs, Anna; University of Pittsburgh, Chemical Engineering

Control over emergence and alignment of transient blisters in thermo-responsive gels using hierarchically patterned substrates

Ya Liu[1,†], Cathy T. Zhang[2,†], Joanna Aizenberg[2,3] and Anna Balazs[1,*]

1. Chemical and Petroleum Engineering Department, University of Pittsburgh, PA, USA
2. Harvard John A. Paulson School of Engineering and Applied Sciences, Harvard University, Cambridge, MA, USA
3. Department of Chemistry and Chemical Biology, Harvard University, Cambridge, MA, USA.

† These authors contributed equally to this work

* To whom correspondence should be addressed. email: balazs@pitt.edu

Abstract

Surfaces with tunable microscale textures are vital in a large variety of technological applications, including heat transfer, antifouling and adhesion. To facilitate such broad-scale use, there is a need to create surfaces that undergo reconfigurable changes in topology and thus, enable switchable functionality. To date, there is a relative dearth of methods for engineering surfaces that can be actuated to change topology over a range of length scales, and hence, form tunable hierarchically structured layers. Combining modeling and experiments, we design a geometrically patterned, thermo-responsive poly N-isopropylacrylamide gel film that undergoes controllable hierarchical changes in topology with changes in temperature. At the bottom, the film is covalently bound to a solid, curved substrate; at the top, the film encompasses longitudinal rectangular ridges that are oriented perpendicular to the underlying cylindrical curves. At temperatures below lower critical solubility temperature (LCST), the swollen gel exhibits 3D variations in polymer density and thickness defined by the gel's top and bottom topography. As the temperature is increased above LCST, the interplay between the upper ridges and lower curves in the gel drives non-uniform, directional solvent transport, the nucleation and propagation of a phase-separated higher-density skin layer, and the resulting pressure buildup within the film. These different, interacting kinetic processes lead to an instability, which produces transient microscopic blisters in the film. Through simulations, we show how tuning the width of the ridges modifies the propagation of a skin layer and creates localized pressure build-up points, which enables control over the emergence, distribution, and alignment of the microscopic blisters. Additionally, we provide a simple argument to predict the size of such microscopic features. Experiments confirm our predictions and further highlight how our computational model enables the rational design of topological transitions in these tunable films. The development of actuatable, hierarchically structured films provides new routes for achieving switchable functionality in actuators, drug release systems and adhesives.

Introduction

The ability to precisely tune and manipulate the way surfaces interact with their immediate environment has important health,[1] energy,[2] and economic implications.[3] Motivated

by the desire to reconfigure surfaces for changing environments, there has been significant interest in developing stimuli-responsive polymeric surfaces, which can be triggered using an external stimulus to exhibit novel, switchable functionality.[4] Manipulating the topology of stimuli-responsive surfaces[5, 6]is vital[7-10]to tailoring the surface for functions ranging from adhesion and friction,[10] to heat transport,[2] to particle transport[11] and bioadhesion[12]. The dimensions, geometry, and hierarchical structure of a surface all affect these functions and indeed, many surfaces can now be designed to exhibit switchable feature sizes[13] and changeable fundamental geometry.[14] Nonetheless, there is still a relative dearth of approaches for creating hierarchically structured, reconfigurable surfaces whose features can be controlled across multiple length scales. Here, we combine modeling and experiments to design multilayer films consisting of a gel and a rigid substrate, where the topology of both the top and bottom layers are shaped simultaneously to encompass distinct geometric patterns. The spatial and temporal interplay between the patterned gel and an external stimulus gives rise to controllable non-equilibrium behavior, which produces films with three-dimensional hierarchical morphologies. This level of control over the geometric patterning and system's dynamics permits the responsive gels to be tailored across the micro- and macro-scales and thus, the approach could be used to design hierarchical, reconfigurable surfaces that are optimally designed for switchable adhesion, antifouling and cell manipulation.

Stimuli-responsive gels have been studied extensively for forming switchable morphologies[15, 16] due to their significant expansion and contraction with small changes in stimuli. The global mutability of these gels is mediated by the physical properties of the constituent polymers, because the solubility and phase behavior of these polymers are sensitive to the external stimuli.[17] For example, under appropriate heating conditions, changes in polymer solubility can lead to phase separation at the gel's surface that affects the transport of water out of the system; the removal of water then in turn influences the overall flexibility of the network. These coupled dynamic interactions can also give rise to instabilities and gradients in polymer density and hydrostatic pressure[18, 19] that produce distinct deformations in the gel's surface. For instance, when thermoresponsive gels containing poly-*N*-isopropylacrylamide (pNIPAAM, lower critical solution temperature, LCST ~32°C) are heated at sufficiently high ramp rates to temperatures above 35°C in water, morphological blisters (micron scale bumps) appear in the surface of the gel. [17, 19]

We recently showed that the spatial localization of such surface blisters can be tuned by covalently bonding the pNIPAAm gel layer to an underlying rigid, structured substrate.[17] The structured substrate affects both the degree of swelling of the gel, and the spatiotemporal dynamics of polymer densification and hydrostatic pressure development within the gel during contraction. The latter two processes dictate the sequence of topographical changes that occur when the temperature is ramped over 35°C and cause transient morphological blisters to be localized to well-defined regions on the surface of the gel.[17]

Building on these studies, we attempt to create more controllably architected layers by patterning both the bottom and the top surface of the gel and thus programming its complex topological reconfigurations. Figure 1 shows an example of such structure formation: the thermoresponsive pNIPAAM gel is cured on the rigid, curved substrate with one-dimensional cylindrical bumps (oriented along the x direction) under the confinement of a microstructured mold with rectangular ridges oriented perpendicular to the grooves on the bottom surface (along the y direction). This form of patterning creates structural heterogeneities and variations in the

gel thickness in both the lateral and vertical directions. Though the template and microstructured mold individually exhibit topological variations in only *x* and *y*, respectively, the preswollen gel cured between the template and mold exhibits continuous variations in height (*z* direction) along both *x* and *y*, and when submerged in water at room temperature, the swollen gel displays complex topology and curvature gradients in all three dimensions.

As we describe below, the dynamics of forming three-dimensional (3D) gradients in this patterned gel gives rise to hierarchically actuatable features with tunable anisotropy. Through simulations, we specifically show how the formation and propagation of a skin layer, and the directional passage of water within the gel are influenced by the width of the ridges on the gel's top surface. Additionally, we find that regulating the rate of skin layer propagation in the *x* and *y* directions permits control over the appearance and directionality of transient microscopic blisters. Based on the mechanical properties of the skin layer and emergence of hydrostatic pressure, we propose a simple argument to estimate the dimensions of these blisters. The modeling studies provide guidelines for achieving control of the overall topology of the gel layer through architecting the boundaries of the gel. The corresponding experiments support the simulation results and suggest a path forward for the rational design of hierarchically actuatable topographies from stimuli-responsive gels.

Methods and Materials

Computational approach

As illustrated in Fig. 1, we model a thermo-responsive gel (colored in blue) that is attached to a solid, curved substrate (in red). Viewed in the *xz*-plane, the substrate resembles a truncated circle with length $L = 100$ and height $h_b = 28$ in units of the lattice spacingL_0, where $L_0 = 5\mu m$ (see below). The bottom of the equilibrated gel layer fills the vacancy between the bumps to form a $500\mu m \times 150\mu m \times 350\mu$m rectangular prism with a thin gel layer on the edge (Fig. 1B; $h_t = 10\mu$m). This setup was studied in our previous work [17] to probe the dynamic, synergistic interactions that can occur between a deformable gel coating and solid substrate. Notably, such coatings are ubiquitous in manufactured materials and goods; thus, understanding this interfacial behavior is vital for a range of technological applications. In particular, we found that when the gel collapses under a rapid ramping to a high temperature ($T \geq 36$ °C with a rate 5°C/min), the gel phase-separates into an upper skin layer of high polymer volume fraction ($\phi \approx 43\%$) and a lower region of low polymer volume fraction ($\phi < 10\%$). The formation of the skin layer begins on the thin gel layer above the bump in this substrate and propagates to the thicker gel region at the center of the crevice.[17] The inhomogeneity in the thickness of the gel induces a gradient in the hydrostatic pressure. Regions of high pressure (near the center of the crevice) eventually deform the gel surface by forming transient water blisters, which burst through the skin layer.[20, 21] This process is reversible and controlled by the propagation of the skin layer and thus, the geometry of the underlying substrate. (If the shape of the substrate, for example, is a truncated circle with a different curvature than in Fig. 1 or a triangular structure with a downward-pointing tip, the kinetics of the process will remain qualitatively the same as long as the geometries induce similar pressure gradients.) To gain greater insight into the distinct, interfacial self-organization and potentially augment the functionality of the gel coating, we now extend our previous study [17] by creating hierarchically structured gel layers that are cured in the presence of the curved substrate and an overlying mold, which introduces ridges protruding away from the top of the gel layer.

To carry out this study, we implement the gel lattice spring model (gLSM), which is a finite element method that allows us to numerically solve the discretized equations for the elastodynamics of the gel. The structural evolution of the local volume fraction of polymer, ϕ, is governed by the following continuity equation[22, 23]:

$$\frac{\partial \phi}{\partial t} = -\nabla \cdot (\phi \mathbf{v}^{(p)}), \quad (1)$$

where $\mathbf{v}^{(p)}$ is the polymer velocity. All equations are presented in the dimensionless form, assuming that length and time are measured in the respective units of L_0 and T_0 (see below). We assume that it is solely the interdiffusion of the polymer and solvent that contributes to the gel dynamics and neglect the net velocity of the polymer-solvent system.[24] The latter assumption is specified through the following equation:

$$\phi\mathbf{v}^{(p)} + (1 - \phi)\mathbf{v}^{(s)} = 0, \quad (2)$$

where $\mathbf{v}^{(s)}$ is the velocity of the solvent. The dynamics of the polymer network is taken to be purely relaxational; [22, 23] consequently, the elastic forces acting on the deformed gel are balanced by the frictional drag due to the relative motion of the solvent. This force balance is expressed as:

$$\nabla \cdot \hat{\boldsymbol{\sigma}} = v_0(k_BT)^{-1}L_0^2/T_0\zeta(\phi)(\mathbf{v}^{(p)} - \mathbf{v}^{(s)}) \quad (3)$$

where $\hat{\boldsymbol{\sigma}}$ is the dimensionless stress tensor (measured in units of $v_0^{-1}k_BT$), v_0 is the volume of a monomeric unit within the chains, and T is temperature.[24] The prefactor $v_0(k_BT)^{-1}L_0^2/T_0$ in front of $\zeta(\phi)$ in eq. (3) is used to write this equation in dimensionless form. The polymer-solvent friction coefficient, $\zeta(\phi)$, is approximated as:[2]

$$\zeta(\phi) = \zeta(\phi_0)(\phi/\phi_0)^{3/2} \quad (4)$$

where ϕ_0 is the local volume fraction of the polymer in the undeformed gel. This approximation is valid in the semi-dilute and intermediate regimes (i.e., $\phi < 0.5$, which is always satisfied in the following calculations). If the stress tensor $\hat{\boldsymbol{\sigma}}$ is known, then Eqs. (2)-(4) give:

$$\mathbf{v}^{(p)} = \Lambda_0(1 - \phi)(\phi/\phi_0)^{-3/2}\nabla \cdot \hat{\boldsymbol{\sigma}} \quad (5)$$

where $\Lambda_0 = k_BT(v_0\zeta(\phi_0)L_0^2/T_0)^{-1}$ is the dimensionless kinetic coefficient.

The stress tensor $\hat{\boldsymbol{\sigma}}$ is obtained from the energy density of the deformed gel, $u(I_1,I_2,I_3)$ [25]

$$\hat{\boldsymbol{\sigma}} = 2I_3^{-1/2}(w_2I_2 + w_3I_3)\hat{\mathbf{I}} + 2I_3^{-1/2}w_1\hat{\mathbf{B}} - 2I_3^{1/2}w_2\hat{\mathbf{B}}^{-1} \quad (6)$$

Here, $\hat{\mathbf{I}}$ is the unit tensor and $\hat{\mathbf{B}}$ is the left Cauchy-Green strain tensor. The invariants of this strain tensor, I_i (i=1,2,3), are specified as: $I_1 = tr\hat{\mathbf{B}}$, $I_2 = \frac{1}{2}\left[(tr\hat{\mathbf{B}})^2 - tr(\hat{\mathbf{B}}^2)\right]$, $I_3 = \det\hat{\mathbf{B}}$. Additionally, $w_i = \frac{\partial}{\partial I_i}u(I_1,I_2,I_3)$.

The energy density $u(I_1,I_2,I_3)$ consists of the elastic energy density associated with the deformation of the gel, u_{el}, and the polymer-solvent interaction energy density, u_{FH}:

$$u = u_{el}(I_1,I_3) + u_{FH}(I_3) \quad (7)$$

The elastic energy u_{el} describes the rubber elasticity of the crosslinked polymer network[26, 27] and is proportional to the crosslink density in the undeformed polymer network c_0:

$$u_{el} = \frac{c_0v_0}{2}(I_1 - 3 - \ln I_3^{1/2}) \quad (8)$$

The expression for u_{FH} takes the following Flory-Huggins form: [25]

$$u_{FH} = I_3^{1/2}[(1 - \phi)\ln(1 - \phi) + \chi_{FH}(\phi,T)\phi(1 - \phi)] \quad (9)$$

Here, $\chi_{FH}(\phi,T)$ is the polymer-solvent interaction parameter. The term $I_3^{1/2} = \phi/\phi_0$ appears in the equation because the energy density is defined by a unit volume in the undeformed state.[22]

Substituting Eqs. (7)-(9) into Eq. (6) yields the following relationship between the stress ($\hat{\boldsymbol{\sigma}}$) and strain ($\hat{\mathbf{B}}$) tensors:

$$\hat{\boldsymbol{\sigma}} = -P(\phi)\hat{\mathbf{I}} + c_0v_0\frac{\phi}{\phi_0}\hat{\mathbf{B}} \quad (10)$$

The pressure $P(\phi)$ is defined as

$$P(\phi) = -\left[\phi + \ln(1-\phi) + \chi(\phi)\phi^2\right] + c_0 v_0 (2\phi_0)^{-1} \quad (11)$$

with $\chi(\phi) = \chi_0 + \chi_1\phi$. $\chi_0(T) = (\delta h - T\delta s)/k_B T$ with δh and δs being the respective changes in the enthalpy and entropy per monomeric unit of the gel. [28]

We assume that the bottom gel sample is adhered to a surrounding glass chamber, which are arranged in the *xy* and yz plane. Therefore, in the *xy* (yz) plane, the velocity of boundary nodes for the gel satisfy the condition $v_z^p(v_x^p) = 0$. The no slip boundary condition is imposed on the interface between the gel and curved substrate. The free boundary condition is applied to the top gel ridge since there is no restriction.

The above equations and imposed boundary conditions are solved numerically using the gLSM,[26] wherein a 3D deformable gel is represented by a set of general linear hexahedral elements. Initially, the sample is undeformed and consists of $(L_x - 1) \times (L_y - 1) \times (L_z - 1)$ identical cubic elements, where L_i is the number of nodes in the *i*-direction, *i* = *x*, *y*, *z*; the linear size of the elements in the undistorted state with $\phi_0 = 0.129$ is set to $L_0 = 1$. The solid bumpy substrate is modeled by frozen gel nodes; the velocities of the frozen nodes is to zero and polymer volume fraction is fixed at $\phi_{bump} = 1$.

We utilize parameter values that are based on the experimental data for poly(N-isopropylacrylamide) (PNIPAAm), which displays a LCST.[28] The polymer volume fraction in the undeformed gel is set to $\varphi_0 = 0.129$ and the crosslink density in the undeformed polymer network is $c_0 = 5.76 \times 10^{-4}$ (unless specified otherwise). For the gel-solvent interaction parameters, we set $\chi_1 = 0.518$, and $\chi_0(T) = \frac{\delta h - T\delta s}{k_B T}$, where $\delta h = -12.4 \times 10^{-14}$, and $\delta s = -4.7 \times 10^{-16}$. In Eq. (5), we use the dimensionless kinetic coefficient $\Lambda_0 = 100$.[29, 30] We set our units of length and time to be $L_0 = 5\mu m$ and $T_0 = 1.25s$, respectively, to ensure the diffusion coefficient $L_0^2/T_0 = 2 \times 10^{-11} cm^2 s^{-1}$.[31] The physical size of the system with $100 \times 70 \times 30$ elements at 31℃ is $500\mu m \times 350\mu m \times 150\mu m$. Hence, the length of the truncated circle forming the bump (Fig. 1a) is $500\mu m$ and height $140\mu m$; the height of gel ridge is 50 μm and the thickness of the gel on the top of the bump is $10\mu m$. From here in, the simulation quantities are presented in the physical units (time measured in seconds and length in microns) to allow the reader to correlate the model parameters to the experiments.

Materials

Lenticulated plastic sheets (50 lines per inch, with bump-to-bump pitch ~500 μm) were purchased from Pacur and Lenstar. Epoxy OG178 was purchased from Epotek. Trichloro(1H,1H,2H,2H-perfluorooctyl)silane (13F-silane), glycidyl methacrylate (GMA), polyethylene glycol diacrylate (PEGDA, Mn 700), Darocur 1173, ethylene glycol and 1-butanol were used as received from Sigma Aldrich. Pyrromethene dye 546 was obtained from Exciton. N-Isopropylacrylamide (NIPAAm) monomer was purchased from Sigma Aldrich and recrystallized in 1 : 1 hexane/toluene mixture overnight at 4°C to remove impurities. Alkyne-functionalized BODIPY-R6G fluorescent dye was purchased from Lumiprobe.

Covalent bonding of epoxy ridges to glass coverslips

Corrugated template created from epoxy resin was fabricated using a method described previously. [17] In brief, lenticulated structures obtained from Lenticular lens plastic sheets (50LPI) were plasma cleaned, silanized in 13F vapor silane under desiccated vacuum conditions and used

as masters for molding. PDMS (Sylgard, base : curing 10 : 1) was poured onto the masters, cured for 2 h at 70°C and peeled off the plastic bumps to reveal PDMS inverse replicas of the bumps. A 50 mm base layer of epoxy mixture was UV-cured (Dymax Model 2000 Flood UV Curing System, light intensity of 18 mW cm2 for 5 mins) under the confinement of a PDMS slab onto 22 mm plasma-treated square glass coverslips. After peeling the PDMS slab off the surface, epoxy bumps were cured on the epoxy base by pressing 1 cm square PDMS inverse replicas of lenticulated bump structures to the surface and infiltrating with epoxy-GMA mixture through capillary filling. The ensemble was UV-cured for 5 mins and the PDMS molds were subsequently peeled off.

Covalent bonding of microstructured gel to epoxy template

Microstructured silicon wafer molds were prepared using conventional photolithography approaches. In brief, adhesion promoter (HMDS) and positive i-line photoresist (SPR700-1.0, about 2 μm height) were spin-coated onto a clean wafer, soft-baked at 95°C for 60 s, patterned using a direct write laser tool (Heidelberg, Maskless Aligner, 405 nm laser at about 125 mJ cm^{-2} s^{-1}), hardened at 115 °C for 60 s, and developed in developer CD-26 for around 90 s. The photoresist-patterned silicon wafer was then ion-etched under optimized Bosch conditions (SPTS Technologies) to nominal height and rinsed in acetone/isopropanol to remove residual photoresist. The resulting silicon microstructures were treated with plasma and passivated with 13F-silane under vacuum for more than 6 h. The silicon masters were then used to prepare polydimethylsiloxane (PDMS) negative moulds. PDMS prepolymer (base-to-hardener ratio of 10:1, wt/wt) was poured onto the master, cured at 70°C for 2 h, and peeled from the masters to obtain negative moulds. PDMS negative moulds were stored in 13F-silane vapour environment for more than 3h.

The microstructured PDMS molds were overlaid on top of the epoxy ridges, and gel solution was infiltrated into the cavities between the PDMS mould and the epoxy ridges. The ensemble was UV-cured (Dymax Model 2000 Flood UV Curing System, light intensity of 18 mW cm^2 for 5 min). Subsequently, the assembly was submerged in water, and the PDMS mould was gently released using a pair of tweezers. The assembly remained in water for at least 12 h before testing to release any uncured monomer.

Confocal imaging of the gel during heating

To visualize changes in surface morphology that occur as the temperature is changed, the sample was imaged in a thin flowcell with a glass window (channel height over the surface channel ~350 μm) placed on a feedback-controlled resistive heating stage controlled by a PID temperature controller (Instec STC200 precision temperature controller) and cooled by water pumped from an ice-water bath (T = 0°C). Prior to all experiments, the top of the stage temperature was carefully calibrated with a digital thermometer (Omega HH1384) equipped with a K-type. Thermocouple to within 0.3°C of the setpoint temperature indicated on the temperature controller. For each experiment, the heating stage was heated to 37°C at 5°C/min, and the fluorescence of the system was tracked for at least 10 minutes. Under these conditions, the flowcell equilibrates to the temperature of the heating stage within a few seconds. To obtain side view cross-section images, fluorescence confocal z-stack images were collected at t = 450 s (Zeiss upright LSM 510, 20 water objective, 0.5 NA, lex = 88 nm, 1 Airy unit pinhole) with separate channels for reflected laser light (lambda = 488 nm), fluorescently labeled epoxy (pyrromethene 546), and hydrogel fluorescence (BODIPY-R6G).

Results and Discussion

Modeling the gel topology. We first performed simulations to investigate the range of behavior that can be exhibited by a multilayer composite system containing a pNIPAAM film patterned with rectangular ridges of different widths (w) on the top surface and covalently bound to a rigid, curved substrate at the bottom. The details of the simulation are provided in the *Methods* section. Briefly, the gel is initially equilibrated at $T = 31°C$; it is then cooled below the critical transition temperature to $T = 22°C$ and equilibrated at this temperature for 2500s. Under these conditions, the gel swells to form the structure in Figs. 2A and B (top view). To aid in visualizing the system, we plot only the portion of the curved surface (in red) that lies close to the bound gel layer. For relatively narrow ridges $w_{ridge} = 50\mu m$ and $100\mu m$, we simulate the presence of both ridges, which lie sufficiently far apart (greater than $50\mu m$) to avoid direct contact during swelling. Thus their mutual interaction can be neglected. When w_{ridge} is increased to $250\mu m$ and $500\mu m$, we model the ridge as a single overlying layer, allowing us to save computation time; the behavior in one wide ridge captures the behavior observed experimentally, as discussed further below. (In the latter cases, the width of solid bump w_b is chosen to be $30\mu m$ wider than the ridge, i.e., $230\mu m$ and $530\mu m$, respectively). The color bar in Fig. 2 indicates the polymer volume fraction in the gel.

The hierarchically structured gels shown in Fig. 2 display two distinct morphological features. First, the portions of the thermo-responsive gel that are in contact with the curved surface display an inhomogeneous degree of swelling: the portion near the crevice, which is the strip between the two bumps, undergoes a greater temperature-dependent change in height than the thin layer near the top of the bumps due to the significantly higher amount of polymer in this region. Second, the deformation of the protruding ridge is influenced by a competition between the topology of the underlying gel and the inherent phase behavior of the LCST gel.

At $T = 22°C$, for $w_{ridge} = 50\mu m$ and $100\mu m$, the deformation of the ridge is mainly due to the stress generated by the underlying swollen gel at the crevice. Careful inspection of Figs. 2B (i) and (ii) shows that the polymer concentration in the center of the gel ridge is relatively lower (dark blue in the color bar) than at the edges (lighter blue), indicating that the center of the ridge is stretched in the lateral direction by the underlying distended gel. For an even narrower width ($w_{ridge} = 25\ \mu m$ as shown in Fig. S1), the ridge forms a wrinkled structure that is similar to instabilities observed in films that are mechanically deformed.[24] As the ridge width is increased to $w_{ridge} = 250\mu m$ and $500\mu m$, the inherent phase behavior of the LCST gel plays a dominant role in dictating the structure of the layer. Namely, the entire layer is swollen at $T = 22°C$, with the width reaching a maximum as it bulges out in the middle of the two lateral edges (Fig. 2B (iii) and (iv)) where the gel has the greatest freedom to expand.

Previously, we showed that when the temperature is ramped up to at $T = 37°C$ (above the LCST) at a rate of 5°C/min, the gel collapses and phase-separates into a relatively dense skin layer, with a polymer volume fraction of $\varphi \approx 43\%$, and an underlying region with a lower polymer volume ranging from ~12% close to the bump sites to ~7% at the crevice sites.[17] The denser, less permeable skin layer inhibits the penetration of water that is expelled when the shell collapses. Consequently, the water is preferentially squeezed along the x and y directions in Fig. 2, with a higher water concentration being localized above the crevice (since there is more free volume in this region than the narrow layer under the bump). The preferential accumulation of

water causes a localized buildup in the hydrostatic pressure, which leads to the formation of small blisters, or "bubbles" on the gel surface.

To gain insight into how the boundaries introduced by the gel ridges could affect bubble formation, here we examine the evolution of the skin layer for different widths of the ridge. Figures 2C and 2D reveal the respective side and top view of the gel at $T = 37°$ for different values of w_{ridge}. The temperature is ramped up at a rate of 5°C/min, leading to the collapse of gel. For $w_{\text{ridge}} = 50\mu m$, the skin layer forms quickly and covers the entire surface of the ridge at t = 653.75s (Fig. 2D (i)); the side walls (along the y-direction) still display blue regions with low polymer volume fraction. Thus, we expect that the water expelled from the collapsing gel would leak out of the side wall (along y) without forming blisters on the surface. As the ridge width is increased to $W_t > 50\mu m$, the skin layer near the side walls (along y) develops faster than on the top surface of the ridge, as evidenced by the relative polymer volume fractions in the system (see color bar). Consequently, the expelled water is forced to escape through the top surface of the ridge (areas of light blue) as the gel collapses. For $w_{\text{ridge}} = 100\mu m$ at t = 656.25s (Fig. 2D (ii)), regions of low polymer fraction on top of the ridge display an anisotropic elliptical shape, with the long axis along the x-direction. When the ridge width is increased to $w_{\text{ridge}} = 250\mu m$ at t = 661.25s, the blue region on the ridge top adopts a more isotropic shape (Fig. 2C (iii)). When $w_{\text{ridge}} = 500\mu m$ at t = 661.25s, the region of low polymer volume fraction changes orientation, forming an anisotropic shape along the y-direction (Fig. 2D (iv)).

The formation of these different shapes can be explained by the development of the skin layer, which we obtain by measuring the propagating velocity at the "frontier", which constitutes the line separating the regions of low (blue) and high (orange) polymer volume fraction on top of the ridge. Given the symmetry of the frontiers in Figs. 2B-2D, we adopt polar coordinates, with the origin being at the center of the low polymer volume region (in blue) and the reference direction being along the x-axis. The frontier is evaluated at 90 sections, which are separated by a distance of four angular degrees. A point in the frontier satisfies two conditions: 1) the polymer volume fraction at the site is greater than 0.4, and 2) the site lies closest to the origin within the section. As shown in Fig. 3A, the frontier (marked in red) is consistent with the structure of the skin layer shown in Fig. 2D.

After defining the frontier in each time frame, the propagating velocity is obtained by measuring the displacement of the frontier grid point (within a given section) in two consecutive time frames, as shown in Fig. 3A. Figure 3B shows the temporal evolution of the horizontal v_h (black) and vertical v_v (red) propagating velocity. Here, v_h is averaged over the velocity on grids located in polar angles [-3°, 3°] and [177°, 183°], and v_v in [87°, 93°] and [267°, 273°]. When the gel relaxes above the critical temperature, the contraction of the gel is governed by the collective diffusion of the polymer relative to the solvent. Time for a diffusive process scales as H^2, where H is the characteristic height of the gel. Thus the velocity (and hence the rate of gel contraction and the development of the skin layer) scales as $(1/H^2)$, where the numerator represents a skin layer that is equal to the grid size. Since the geometry of the underlying bump is invariant along the y direction (in any x-z plane), v_v should be insensitive to both time and ridge width. As shown in Fig, 3B, the plot of v_v as a function of time (red curve) is relatively flat, with a magnitude that remains close to one. On the other hand, the gel thickness h increases along the x-direction toward the center of the skin layer (at the center of the surface), and the black curves in Fig. 3B are consistent with the fact that v_h scales as $(1/H^2)$.

This anisotropy in the formation of the frontier allows us to control the shape of this leading edge by altering the ridge geometry since the ratio of the frontier dimension in the x-

direction relative to that in *y*-direction could be estimated as ($\frac{L-2\int v_x dt}{w_{\text{ridge}}-2v_y t}$) at a given time *t*, where *L* is the gel length and w_{ridge} is the ridge width. To obtain this approximation, we note that if the skin layer has been developing for *t* time steps, the skin layer frontier will travel a distance along the *y*-direction that is $\sim v_y t$ since v_y is nearly a constant. The width of the region enclosed by the frontier along the *y*-direction is then $w_{\text{ridge}} - 2v_y t$. Similarly, the frontier will travel $\int v_x$ dt from 0 to t. The dependence of v_x on *t* can be obtained from Fig. 3B. Thus, we obtain the aspect ratio given above. (Note the propagating velocity is well defined during the development of the skin layer, but is not well defined after the skin layer has formed. The calculation is only valid in the certain range of time frames, which are shown in Fig. S2.)

The contraction of gel causes a buildup of hydrostatic pressure, which eventually drives the water to bulge through the skin layer, form bubbles and modify the topology of this layer. As shown in Fig. 4, the region of maximal hydrostatic pressure is coincident with the frontier of the skin layer. This coincidence occurs because the frontier encompasses the greatest changes of the polymer volume fraction and thus leads to the greatest deformation of the gel, as well as the hydrostatic pressure. As the width of the gel is increased, the steepest gradients of these quantities change orientation, with the long axis of the structure changing from the horizontal to vertical. We thus anticipate that the alignment of the formed bubbles will also change; this prediction is confirmed in the experiments described further below.

Our gel lattice spring model (see *Methods*) does not include an explicit description of the solvent molecules (which are instead described by the diffusion terms in the reaction-diffusion equation), and thus cannot be used to directly characterize the formation of blisters such as the location of emergence and size. Such information is critical for dynamically controlling the topography of gel interface.[17] In particular, the dimensionality of blister characterizes the degree of gel local deformation, which is difficult to access in experiments.[17] We thus combine our simulation and the classic theory of elastic membrane to estimate the blister size; the results agree with experimental measurements as discussed further below.

Analog to the blisters formed due to the hydrostatic pressure causing water to bulge through the skin layer, we consider an axisymmetric elastic membrane, which is inflated by injecting water through a circular tube under a uniform pressure, where the strain energy density is applied: [32]

$$W = \frac{E}{2}(I_1 - 3) \tag{12}$$

as shown in Fig. 5. The material constant *E* equals to the shear modulus C^M for thin membrane[33] and I_1 is the trace of left Cauchy-Green deformation tensor. Note Eq. (12) is known as an energy density function for neo-Hookean incompressible material.[22] This model has been successfully applied in the evaluating the size of blister formed on the flat substrate under fluidic pressure[34] or on the surface of cylindrical gel when the gel collpases.[18] Given the undeformed member thickness h_0, uniform pressure *P* and tube radius *R*, the height of circular blister δ reaches equilibrium and follows the relation (Eq. (40) in Ref. 32):[32]

$$\frac{PR}{C^M h_0} = \frac{4\delta/R}{\left(1+(\delta/R)^2\right)}\left(1 - \frac{1}{\left(1+(\delta/R)^2\right)^3}\right). \tag{13}$$

Under the condition of large deformation $\delta \gg R$, we obtain

$$\delta = \frac{4C^M h_0}{P} \tag{14}$$

Note that δ is proportional to $1/P$, suggesting if a blister with large deformation is in the equilibrium state, the pressure inside a larger-sized blister is smaller in magnitude than for a smaller blister. In our study, the skin layer with a high polymer volume fraction is less permeable to the solution[34] and thus plays a role as the thin elastic membrane. The hydrostatic pressure causes water to bulge through the skin layer, forming blister. Therefore the shear modulus is determined by the mechanical properties of the skin layer: $C^M = \frac{1}{2}c_0\frac{\phi_{skin}}{\phi_0}k_bT$,[22] where c_0 is the crosslinking density, ϕ_0 the initial polymer concentration, ϕ_{skin} the polymer concentration in skin layer and k_b the Boltzmann constant. $P = \frac{1}{3}tr(\hat{\boldsymbol{\sigma}})$ is the sum of two contributions including the elasticity of the polymer network and the osmotic pressure.[17] We can measure these quantities from our gLSM simulation such as: $c_0 = \frac{5.4 \times 10^{-4}}{L_0^3}$ with $L_0 = 5\mu m$ the element size, $\phi_0 = 0.129$ and ϕ_{skin}~0.43. Since the presence of blisters is observed in experiments at t = 725s, the corresponding thickness of skin layer is in the order of magnitude of L_0: $c_0 \approx L_0 = 5\mu m$. Since the hydrostatic pressure P is inhomogeneous in the gel (as illustrated in Fig 4), we take its maximum value in the simulation at t = 725s and get $P = 8 \times 10^{-4}\frac{k_bT}{L_0^3}$. Using Eq. 13, we finally obtain the diameter of the emerging elastic balloon: $\delta \sim 42$ μm.

Experimental demonstration of the emergent gel topography. We conducted the following experiments to confirm the spatial localization and dimensions of microscopic blisters predicted by simulations. The rigid, corrugated template underlying the gel was fabricated from epoxy resin doped with glycidyl methacrylate through a double molding process, and the thermoresponsive pNIPAAm gel was covalently bonded to it via UV-curing under the confinement of a microstructured silicone mold structured with periodically spaced rectangular grooves. The grooves were spaced w_g = 256 μm apart and had widths of w_{ridge} = 128 μm, 256 μm and 512 μm. The details of the fabrication process are detailed in Materials and Methods. The structure of the gel before swelling in water is shown in Fig 6A.

Upon submerging in water, the gel-template hybrid surface swelled to exhibit complex topology and curvature variations, shown schematically in Fig. 6Bi. We heated the gel rapidly to 37°C (above LCST) at 5°C/min and used confocal fluorescence microscopy (set to maximum pinhole size, to capture changes within ±50 μm of the top of the gel surface) to track changes in the surface of the gel for 450 s (schematic of the temperature ramp is shown in Fig 6Bii). Under these heating conditions, the gel reaches the setpoint temperature of 37°C within t ~ 180 s, and the surface continues to evolve under a constant external temperature of 37°C. Representative images of the gel surface obtained using confocal microscopy are shown in Fig. 6C at t=0/T=22°C (top row) and at t=450s/T=37°C (bottom row). For gels with w_{ridge} =128 μm, the gel surface changes smoothly with no detectable inhomogeneities. In contrast, for gels with widths of w_{ridge} = 256 μm or 512 μm, circular inhomogeneities of ~50 μm in diameter were observed in the fluorescence intensity of the gel. As shown previously, these structures disappear upon decreasing the temperature below the phase transition temperature, and reappear after ramping the temperature from 22°C back to 37°C (Supplemental video, SV1).

The formation of these inhomogeneities correspond to the formation of microscopic blisters, which we further verified using confocal microscopy. Z-stack images that were acquired

at t=750s after heating began confirm the presence of ~5-10 μm microscale blisters on top of the gel for w_{ridge} = 256μm and 512 μm, as shown in the topographic maps presented as insets in Fig.6C (bottom row). Individual slices of the z-stack image can also be found in SI (Fig. S3). As predicted by the simulations, the formation of the microscopic blisters occurs for w_{ridge} = 256 μm and 512 μm (SI Fig. S4), but not for w_{ridge} = 128 μm, which can be attributed to the slow diffusion of water out of the gel through the surface relative to the rate of the skin layer formation for these two cases. The average diameter of each protruding bump was ~50 μm (SI Fig. S4), which is quite consistent with the ~42 μm value derived by the simulations. We note that the size of the blister is related to the crosslinking density c_0 ($r_0 = \frac{4H_0C^M}{P}$) not only through the shear modulus, but also through the hydrostatic pressure P. Since a gel with a higher crosslinking density is more resistant to deformation, the skin layer is expected to form later, and the pressure P is expected to increase with increases in crosslinking density. The latter observation is confirmed in a recent study of blister formation on a cylindrical gel [18]. Future studies are needed to determine the dependence of the size of the blisters on the crosslinking density, and the slightly larger experimental value compared to the simulations might be explained by the difference in the crosslinking density in the synthesized gel.

Furthermore, experimental data clearly shows that the orientation of the microscopic blisters depends on w_{ridge}. In particular, for the gels with narrower ridges (w_{ridge}=256 μm), an array of microscale blisters appearing upon heating is aligned in the x-direction along the rectangular grooves on the top surface, while for the gels with wider ridges (w_{ridge}=512 μm), arrays of blisters switch to a perpendicular y-direction and develop across the rectangular groove. This result is consistent with the simulations presented above, which show that the skin layer formation and hydrostatic pressure buildup occur more rapidly along the y-direction compared to the x-direction within the narrower gel ridges (for w_{ridge}=256 μm), and as the width of the ridge is increased (for gels with w_{ridge}=512 μm), the steepest gradients of polymer volume fraction in the developing skin and the pressure build-up change orientation.

Conclusion

In this work, we used a combination of simulations and experiments to show how multilayer films consisting of surface-structured stimuli-responsive gels bonded to a curved, rigid substrate can be actuated by stimuli to exhibit 3D, tunable, and hierarchical changes in morphology. Using a model system containing a pNIPAAm gel with rectangular ridges on the top surface oriented perpendicular to bumps on an underlying template, we showed how the gel and gel-template boundaries shape the dynamics of solvent transport, phase separation and skin layer development within the gel when the gel is heated rapidly above its LCST. Our comprehensive modeling shows that the variation in the gel thickness in all three directions defined by the geometry of the gel's top and bottom surfaces leads to the asymmetric diffusion of the solvent, which gives rise to anisotropy in the shape of the skin layer frontier and directionality of hydrostatic pressure gradients. Through experiments, we confirmed that these gradients correspond to the formation of tunable and hierarchically actuatable surface morphologies, with small microscopic blisters emerging on the macroscopic structure of the gel ridges. Importantly, the simulations and experiments show that the size and the orientation of these blisters are defined and can be controlled by the width of the gel ridges shaping the top surface.

Our work points to the crucial role of architecting the geometric boundaries of the gel, to program the transformation pathways of stimuli-responsive gel composite films. Moreover, this

work provides insight into how finite element simulations can be harnessed to guide the development of stimuli-responsive films with designed topological reconfigurations. We anticipate that such hierarchically actuatable topologies will open new avenues toward multifunctionality in actuators, drug release systems and adhesives.

Acknowledgements. *This work is supported by the Center for Bio-Inspired Energy Science (CBES), an Energy Frontier Research Center funded by the U.S. Department of Energy (DOE), Basic Energy Sciences (BES), under award DE-SC0000989.*

References

1. Harding, J. L.; Reynolds, M. M., Combating medical device fouling. *Trends in Biotechnology* **2014,** *32* (3), 140-146.
2. Attinger, D.; Frankiewicz, C.; Betz, A. R.; Schutzius, T. M.; Ganguly, R.; Das, A.; Kim, C.-J.; Megaridis, C. M., Surface engineering for phase change heat transfer: A review. *MRS Energy & Sustainability* **2014,** *1* (1), 4.
3. Schultz, M. P.; Bendick, J. A.; Holm, E. R.; Hertel, W. M., Economic impact of biofouling on a naval surface ship. *Biofouling* **2011,** *27* (1), 87-98.
4. Stuart, M. A. C.; Huck, W. T. S.; Genzer, J.; Müller, M.; Ober, C.; Stamm, M.; Sukhorukov, G. B.; Szleifer, I.; Tsukruk, V. V.; Urban, M.; Winnik, F.; Zauscher, S.; Luzinov, I.; Minko, S., Emerging applications of stimuli-responsive polymer materials. *Nature Mater* **2010,** *9* (2), 101-113.
5. Huang, X.; Sun, Y.; Soh, S., Stimuli-Responsive Surfaces for Tunable and Reversible Control of Wettability. *Adv. Mater.* **2015,** *27* (27), 4062-4068.
6. Kuroki, H.; Tokarev, I.; Minko, S., Responsive Surfaces for Life Science Applications. *Annu. Rev. Mater. Res.* **2012,** *42* (1), 343-372.
7. Erramilli, S.; Genzer, J., Influence of surface topography attributes on settlement and adhesion of natural and synthetic species. *Soft Matter* **2019,** *15* (20), 4045-4067.
8. Hou, H.; Yin, J.; Jiang, X., Smart Patterned Surface with Dynamic Wrinkles. *Acc. Chem. Res.* **2019,** *52* (4), 1025-1035.
9. Tokarev, I.; Minko, S., Preprogrammed Dynamic Microstructured Polymer Interfaces. *Advanced Functional Materials* **2019,** *30* (2).
10. Kamperman, M.; Synytska, A., Switchable adhesion by chemical functionality and topography. *J. Mater. Chem.* **2012,** *22* (37), 19390.
11. Ionov, L., Actively-moving materials based on stimuli-responsive polymers. *J. Mater. Chem.* **2010,** *20* (17), 3382.
12. Tekin, H.; Ozaydin-Ince, G.; Tsinman, T.; Gleason, K. K.; Langer, R.; Khademhosseini, A.; Demirel, M. C., Responsive Microgrooves for the Formation of Harvestable Tissue Constructs. *Langmuir* **2011,** *27* (9), 5671-5679.
13. Turner, S. A.; Zhou, J.; Sheiko, S. S.; Ashby, V. S., Switchable Micropatterned Surface Topographies Mediated by Reversible Shape Memory. *ACS Appl. Mater. Interfaces* **2014,** *6* (11), 8017-8021.

14. Li, S.; Deng, B.; Grinthal, A.; Schneider-Yamamura, A.; Kang, J.; Martens, R. S.; Zhang, C. T.; Li, J.; Yu, S.; Bertoldi, K.; Aizenberg, J., Liquid-induced topological transformations of cellular microstructures. *Nature* **2021,** *592* (7854), 386-391.
15. Liu, D.; Bastiaansen, C. W. M.; den Toonder, J. M. J.; Broer, D. J., (Photo-)Thermally Induced Formation of Dynamic Surface Topographies in Polymer Hydrogel Networks. *Langmuir* **2013,** *29* (18), 5622-5629.
16. Kommeren, S.; Dongmo, J.; Bastiaansen, C. W. M., Switchable surface structured hydrogel coatings. *Soft Matter* **2017,** *13* (11), 2239-2245.
17. Zhang, C. T.; Liu, Y.; Wang, X.; Wang, X.; Kolle, S.; Balazs, A. C.; Aizenberg, J., Patterning non-equilibrium morphologies in stimuli-responsive gels through topographical confinement. *Soft Matter* **2020,** *16* (6), 1463-1472.
18. Shen, T.; Kan, J.; Benet, E.; Vernerey, F. J., On the blistering of thermo-sensitive hydrogel: the volume phase transition and mechanical instability. *Soft Matter* **2019,** *15* (29), 5842-5853.
19. Chang, Y.-W.; Dimitriyev, M. S.; Souslov, A.; Nikolov, S. V.; Marquez, S. M.; Alexeev, A.; Goldbart, P. M.; Fernández-Nieves, A., Extreme thermodynamics with polymer gel tori: Harnessing thermodynamic instabilities to induce large-scale deformations. *Phys. Rev. E* **2018,** *98* (2), 020501.
20. Shibayama, M.; Nagai, K., Shrinking Kinetics of Poly(N-isopropylacrylamide) Gels T-Jumped across Their Volume Phase Transition Temperatures. *Macromolecules* **1999,** *32* (22), 7461-7468.
21. Boudaoud, A.; Chaieb, S., Mechanical phase diagram of shrinking cylindrical gels. *Phys Rev E Stat Nonlin Soft Matter Phys* **2003,** *68* (2 Pt 1), 021801.
22. Yashin, V. V.; Balazs, A. C., Theoretical and computational modeling of self-oscillating polymer gels. *The Journal of Chemical Physics* **2007,** *126* (12), 124707.
23. Zhang, T.; Yashin, V. V.; Balazs, A. C., Fibers on the surface of thermo-responsive gels induce 3D shape changes. *Soft Matter* **2018,** *14* (10), 1822-1832.
24. Li, B.; Cao, Y.-P.; Feng, X.-Q.; Gao, H., Mechanics of morphological instabilities and surface wrinkling in soft materials: a review. *Soft Matter* **2012,** *8* (21), 5728.
25. Barrière, B.; Leibler, L., Kinetics of solvent absorption and permeation through a highly swellable elastomeric network. *Journal of Polymer Science Part B: Polymer Physics* **2003,** *41* (2), 166-182.
26. Hill, T. L., *An Introduction to Statistical Thermodynamics*. Addison-Wesley: 1960.
27. Onuki, A., *Theory of phase transition in polymer gels*. Springer: 1993; Vol. Transitions I.
28. Hirotsu, S., Softening of bulk modulus and negative Poisson's ratio near the volume phase transition of polymer gels. *The Journal of Chemical Physics* **1991,** *94* (5), 3949-3957.
29. Tyson, J. J., *A Quantitative Account of Oscillations, Bistability, and Traveling Waves in the Belousov-Zhabotinskii Reaction*. Wiley: New York, 1985; p 93-144.
30. Scott, S. K., *Oscillations, Waves, and Chaos in Chemical Kinetics*. Oxford University Press: New York, 1994.
31. Liu, Y.; McFarlin, G. T. t.; Yong, X.; Kuksenok, O.; Balazs, A. C., Designing Composite Coatings That Provide a Dual Defense against Fouling. *Langmuir* **2015,** *31* (27), 7524-32.
32. Long, R.; Shull, K. R.; Hui, C.-Y., Large deformation adhesive contact mechanics of circular membranes with a flat rigid substrate. *Journal of the Mechanics and Physics of Solids* **2010,** *58* (9), 1225-1242.

33. Dos Santos, D. J.; Carastan, D. J.; Tavares, L. B.; Batalha, G. F., 2.03 - Polymeric Materials Characterization and Modeling. In *Comprehensive Materials Processing*, Hashmi, S.; Batalha, G. F.; Van Tyne, C. J.; Yilbas, B., Eds. Elsevier: Oxford, 2014; pp 37-63.
34. Benet, E.; Zhu, H.; Vernerey, F. J., Interplay of elastic instabilities and viscoelasticity in the finite deformation of thin membranes. *Phys Rev E* **2019,** *99* (4-1), 042502.

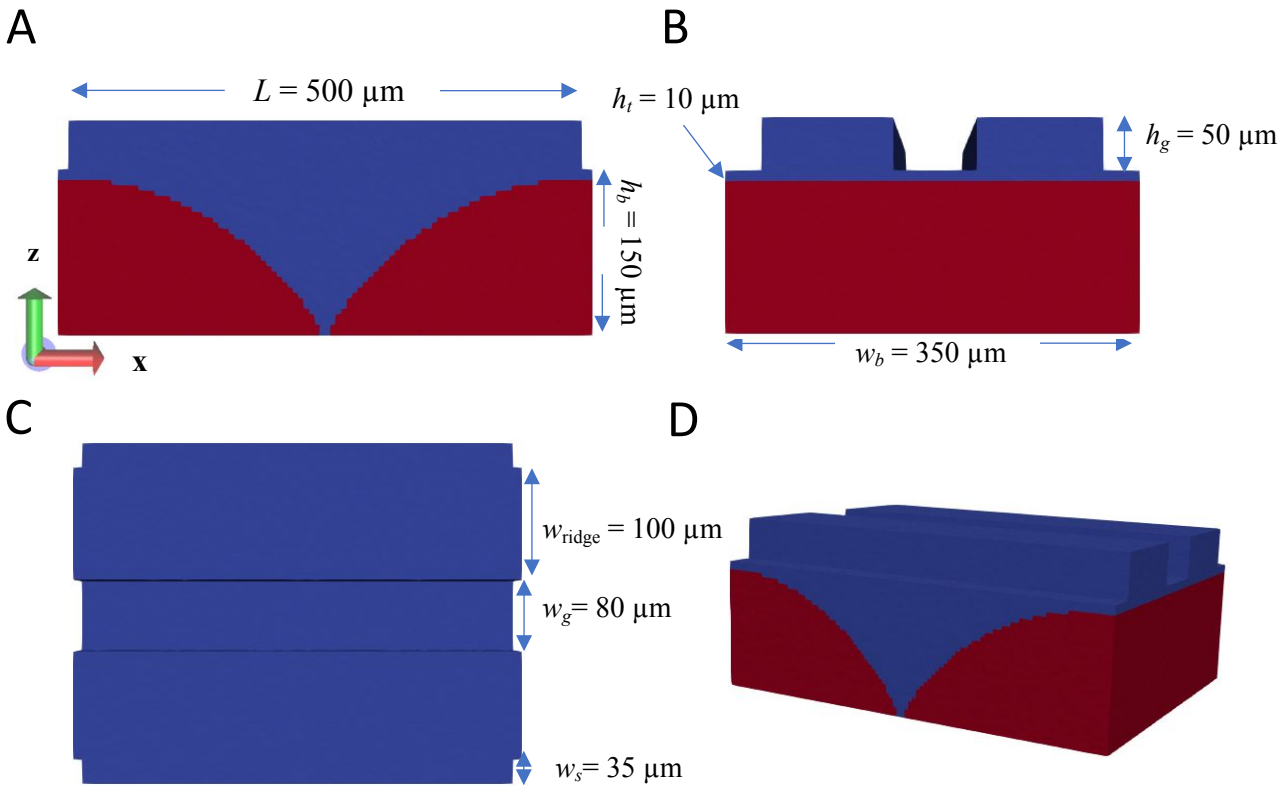

Figure 1: **3D gLSM simulation configuration for a gel confined to a topographically patterned surface with step variations in height z as a function of y.** (A) Front (xz-plane), (B) side (yz-plane), (C) top (xy-plane), and (D) overall view of the structured gel sample (colored in blue) on solid bump (red). The cross section of bump is a truncated circle with length L =500 µm and height h_b = 150 µm. The top gel contains two separated ridges and resembles a canal structure with width w_g = 100 µm , gap w_g = 80 µm and height h_g = 50 µm.

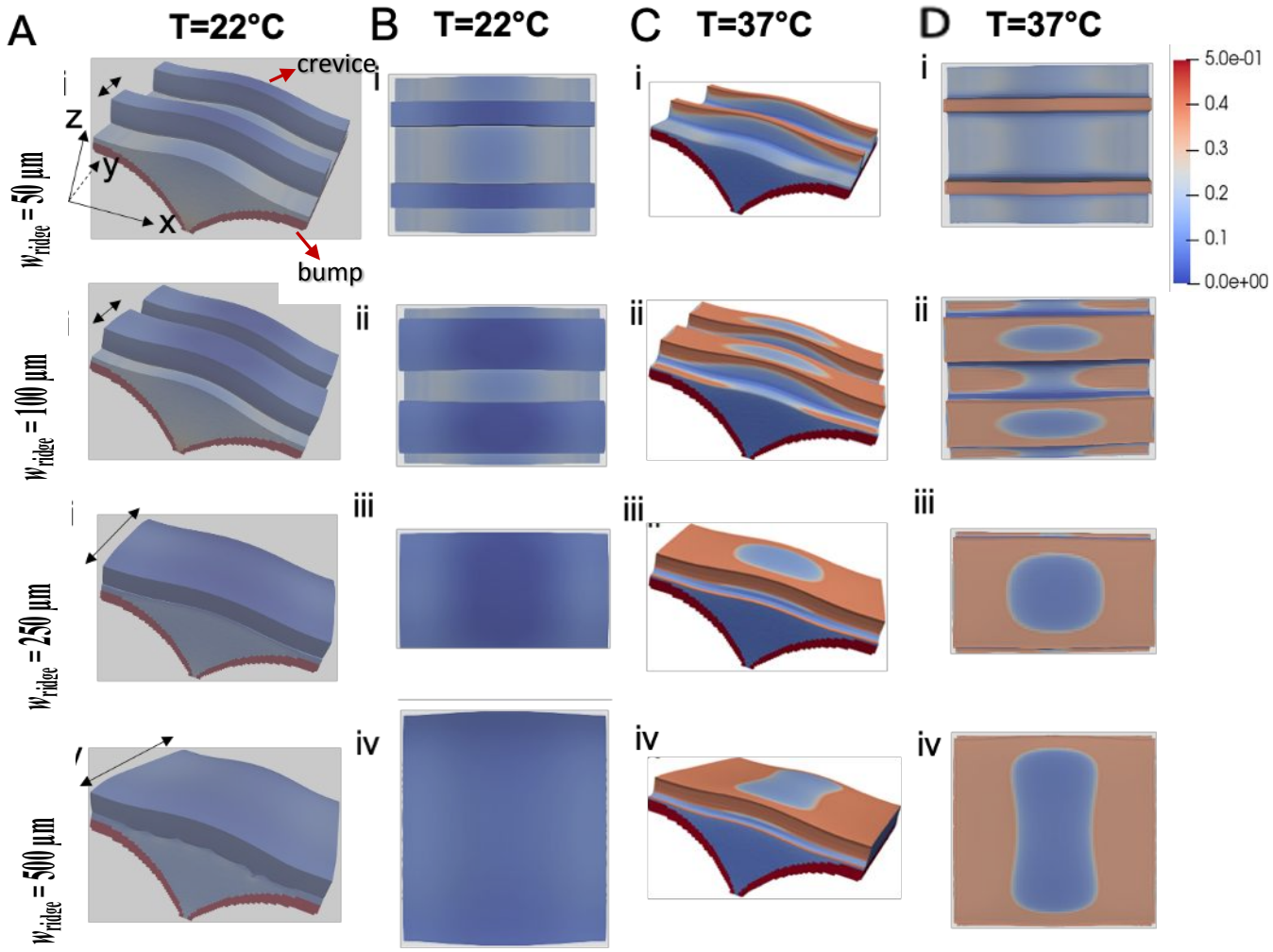

Fig 2. The directionality of skin layer propagation on the surface of the gel depends on the width of the gel ridge when the gel is step ramped quickly from T = 22°C to 37°C. 3D representation (A), top view image at 22°C (B), side view (C) and top view (D) image at T = 37°C for gel with various configuration of ridge widths: (i) w_{ridge}=50 µm (t = 653.75s), (ii) w_{ridge}=100 µm (t = 656.25s), (ii) w_{ridge}=250 µm (t = 661.25s), and (iv) w_{ridge}=500 µm (t = 661.25s) . Color bar represents the polymer volume fraction in the gel.

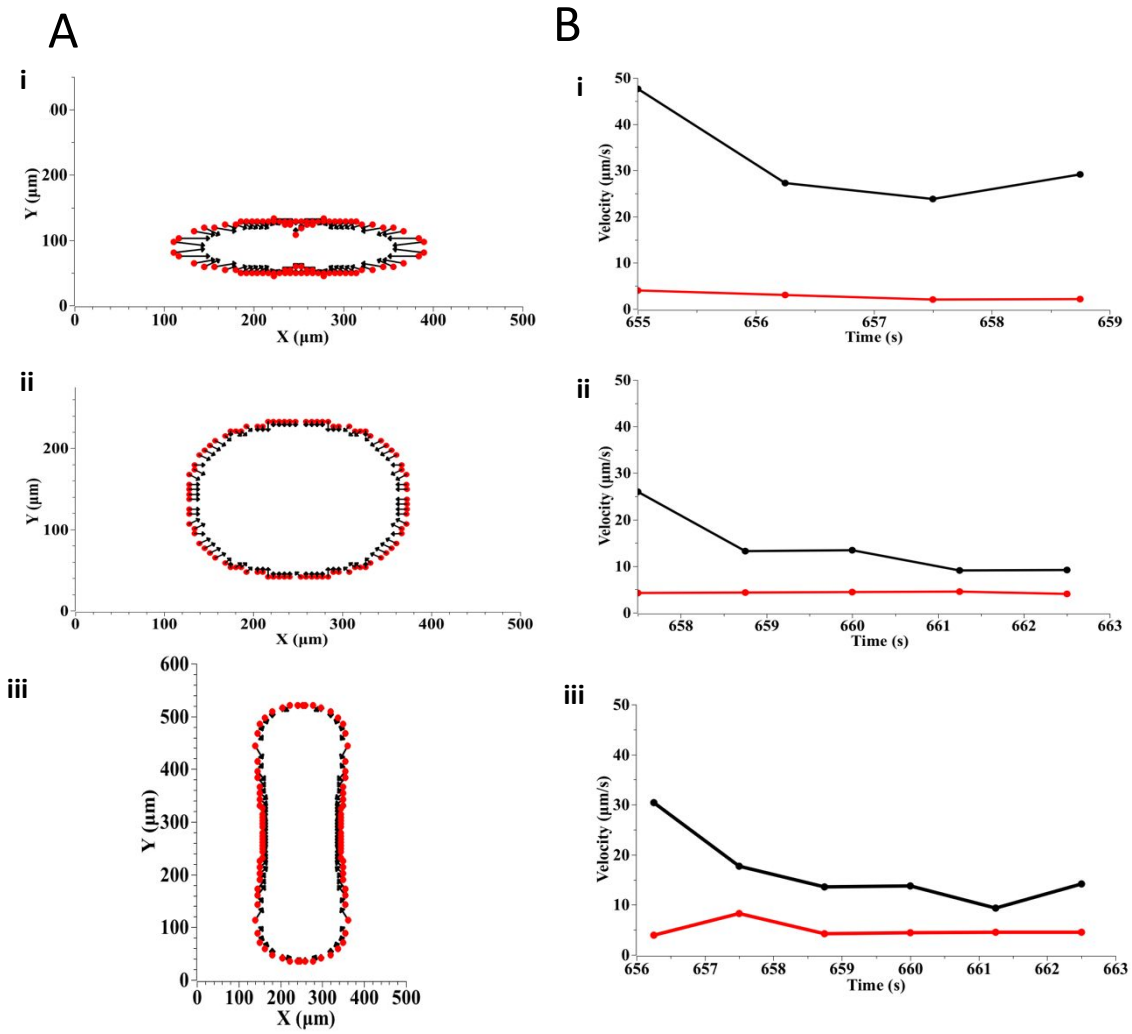

Fig 3. Anisotropy in skin layer formation and propagation in the x and y directions depends on the width of the gel. A. Snapshots of instantaneous velocity field of skin layer propagation for gels with simulation configuration (i) w_{ridge} =100 µm, (ii) w_{ridge} =250 µm and (iii) w_{ridge} =500 µm in the same time frame as shown in Fig. 2D. B. Quantification of growth rate of skin layer in the x direction (black) and y direction (red) for simulation configuration (i) w_{ridge} =100 µm, (ii) w_{ridge} =250 µm and (iii) w_{ridge} =500 µm.

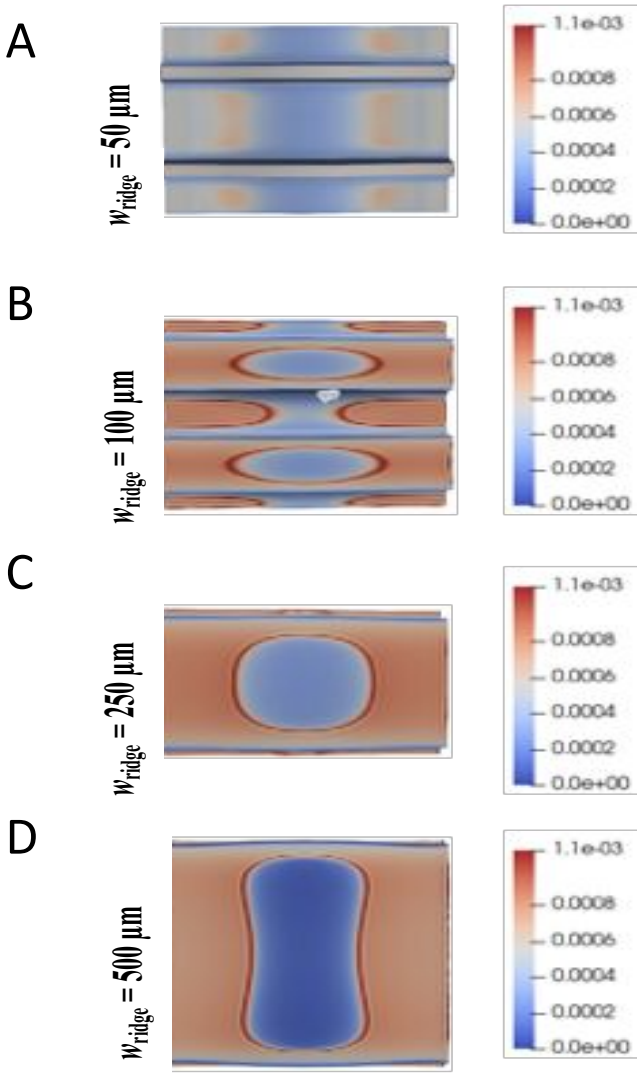

Fig 4. **Anisotropy in hydrostatic pressure buildup due to anisotropic skin layer formation**. $\mathbf{w_{ridge}}$ = 50 µm (A), 100 µm (B), 250 µm (C), and 500 µm (D) in the same time frame shown in Fig. 2D. Color bars represent the hydrostatic pressure in the gel.

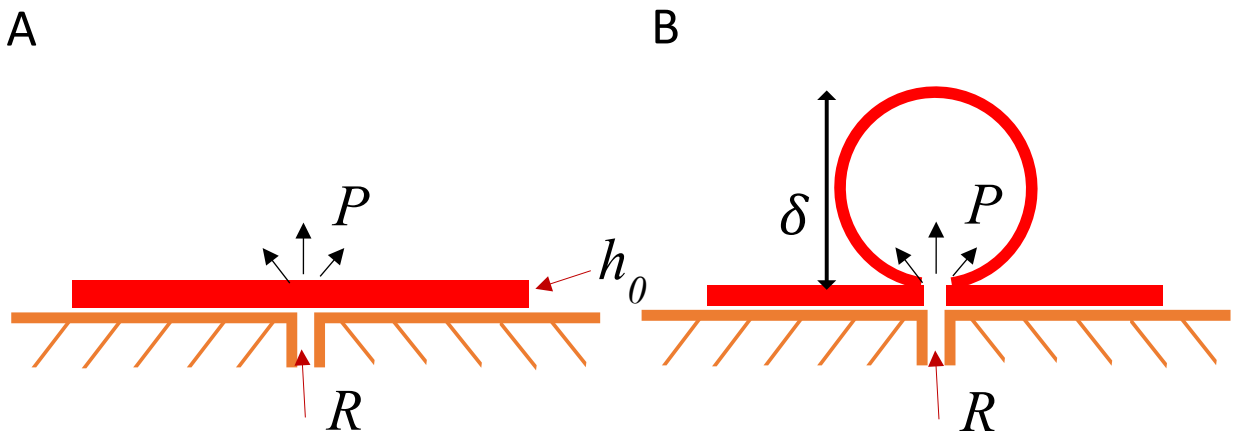

Fig 5. **Elastic theory predicts blister size.** (A) Schematic of film inflated through the tube under pressure. R is the tube diameter and h_0 the thickness of the flat film. (B) Large deformation of film with height δ.

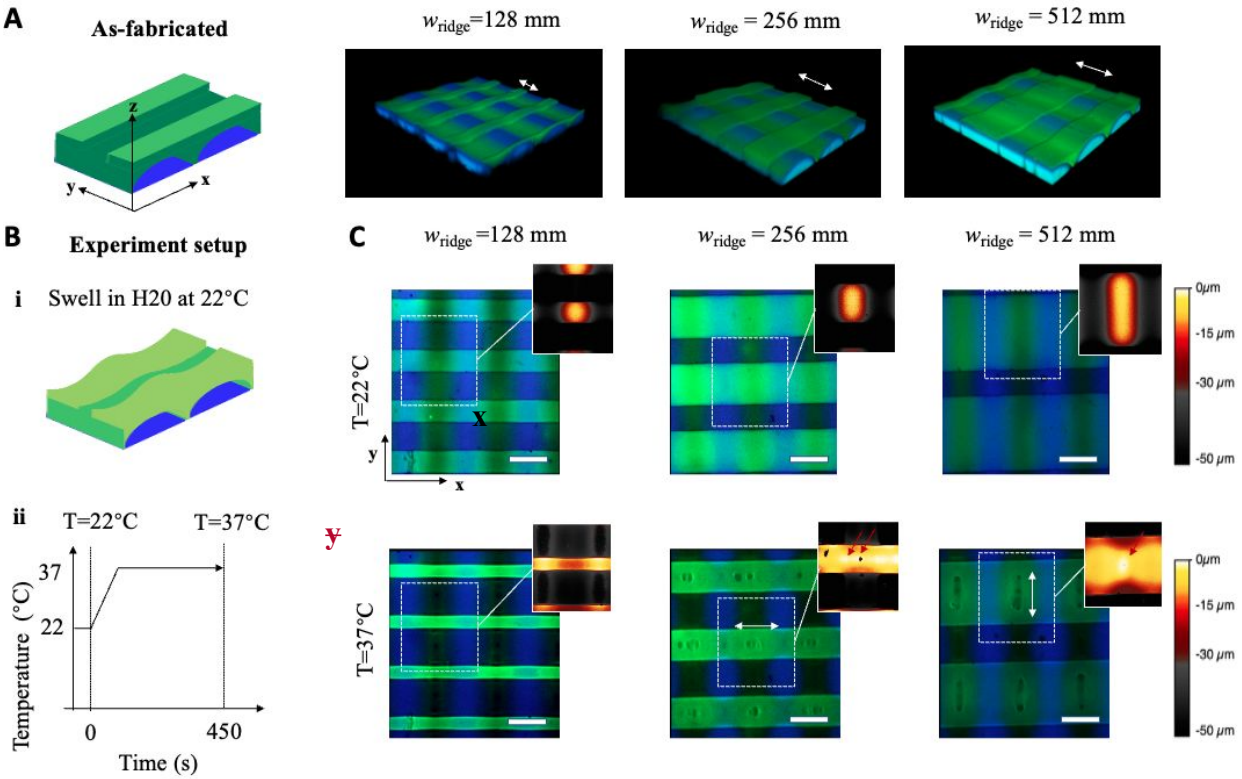

Fig 6. A. Fluorescence z-stack confocal images of samples with patterned gel ridges (stained with BODIPY FL, represented in green) bonded to lenticulated epoxy bumps (stained with Pyrothene, represented in blue) before being swollen in water. Gel ridges are spaced 256 microns apart and were molded with widths of w=128 microns, 256 microns, and 512 microns. B. Schematic of experiment setup. (i) Samples were swollen overnight at 22°C. (ii) Samples were heated to 37°C at a rate of 5°C/min to 37°C, and then allowed to equilibrate at 37°C for 5 minutes. Timelapse topview images were acquired every 2 s throughout the heating process. C. Representative timelapse fluorescence images taken at t=0, T=22°C and t=450s, T=37°C for samples with gel ridge widths of w=128 microns, 256 microns, and 512 microns. Inset: Topography map of a stack confocal images showing the structure of gel ridges obtained from fluorescent confocal z stacks.